

Effects of time-varying flexibility on the propulsion performance of a flapping foil

Cite as: Phys. Fluids **32**, 121904 (2020); <https://doi.org/10.1063/5.0027927>

Submitted: 01 September 2020 . Accepted: 03 December 2020 . Published Online: 24 December 2020

 Guangyu Shi (时光宇),  Qing Xiao (肖青), and  Qiang Zhu (朱强)



View Online



Export Citation



CrossMark

ARTICLES YOU MAY BE INTERESTED IN

[Computational analysis of hydrodynamic interactions in a high-density fish school](#)

Physics of Fluids **32**, 121901 (2020); <https://doi.org/10.1063/5.0028682>

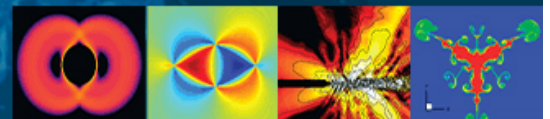
[Optimal chordwise stiffness distribution for self-propelled heaving flexible plates](#)

Physics of Fluids **32**, 111905 (2020); <https://doi.org/10.1063/5.0029806>

[Scaling the vorticity dynamics in the leading-edge vortices of revolving wings with two directional length scales](#)

Physics of Fluids **32**, 121903 (2020); <https://doi.org/10.1063/5.0024213>

Physics of Fluids
GALLERY OF COVERS



Effects of time-varying flexibility on the propulsion performance of a flapping foil

Cite as: Phys. Fluids 32, 121904 (2020); doi: 10.1063/5.0027927

Submitted: 1 September 2020 • Accepted: 3 December 2020 •

Published Online: 24 December 2020



View Online



Export Citation



CrossMark

Guangyu Shi (时光宇),^{1,a)}  Qing Xiao (肖青),¹  and Qiang Zhu (朱强)² 

AFFILIATIONS

¹Department of Naval Architecture, Ocean and Marine Engineering, University of Strathclyde, Glasgow G4 0LZ, Scotland, United Kingdom

²Department of Structural Engineering, University of California San Diego, La Jolla, California 92093, USA

^{a)} Author to whom correspondence should be addressed: guangyu.shi@strath.ac.uk

ABSTRACT

In this paper, we numerically investigate the effects of time-varying bending stiffness on the propulsion performance of a flapping foil using a fully coupled fluid-structure interaction model. The flow field is simulated using a Navier–Stokes solver while the structural dynamics is resolved by a nonlinear beam model. The force generation, the passive deformation, and the flow field of the flexible foil are significantly affected by the time dependency of flexibility. Here, both the actuation at the leading edge and the stiffness of the foil vary sinusoidally, and the phase ϕ between them plays an important role in determining the performance of the foil. At $\phi = 0^\circ$, the maximum time-averaged thrust coefficient can be increased by $\sim 52\%$ whereas the highest propulsion efficiency remains almost the same as that of the foil with a constant flexibility. This is of significance when the size of the wing is often constrained. In addition, the foil with time-varying stiffness generates considerable lift force, which is attributed to the non-symmetrical deformations and deflected vortex-shedding patterns. Finally, the force generation due to added mass is discussed using a simplified model.

Published under license by AIP Publishing. <https://doi.org/10.1063/5.0027927>

I. INTRODUCTION

The dynamics of flapping foils are fascinating and have practical applications in the design of micro-aerial vehicles (MAVs) at low Reynolds numbers.¹ In the past few decades, numerous studies have contributed to this appealing research field.^{2,3} Many previous studies have concentrated on rigid foils undergoing heave and/or pitch motions.^{4–11} For purely plunging foils, it has been revealed that with the increase in flapping frequency, the wake behind the foil transfers from drag-indicative to thrust-indicative, and the motion of the foil creates an effective angle of attack, which causes the resultant force to lean forward, thereby producing thrust.^{12,13} As the frequency further increases, the symmetry of the vortex shedding breaks, and a deflected wake is created, which results in the generation of lift force.¹⁴ The Strouhal number (St) is usually considered an important parameter for the dynamics of flapping foils. Indeed, some previous studies revealed that flapping foils achieved the best performance in the range of $0.25 < St < 0.4$, which is consistent with that of birds, insects, and marine animals in nature.¹⁵ However, it is also reported that the Strouhal number alone is not sufficient to characterize

the propulsion performance of flapping foils.¹⁶ The wake structures and force generation also strongly depend on the reduced frequency and the normalized amplitude.¹⁷

The effects of structural flexibility on the propulsion efficiency of flapping foils have also been widely investigated in many previous papers.^{18–20} The inclusion of material stiffness introduces two important parameters, namely, normalized bending stiffness (K) and mass ratio (\tilde{m}). Heathcote and Gursul²¹ experimentally investigated the propulsion performance of a heaving foil with chordwise flexibility. They found that the thrust coefficient and the propulsion efficiency were functions of the Strouhal number and the phase angle between the imposed heave and the induced pitch motions. Both thrust and efficiency were greatly enhanced if an appropriate degree of flexibility was used. It was also revealed that higher thrust forces were associated with stronger trailing-edge vortices whereas higher efficiencies corresponded to relatively weaker leading-edge vortices. Shoele and Zhu²² numerically examined a skeleton-reinforced flapping wing with non-uniformly distributed stiffness. It was found that a strengthened leading edge could significantly augment the lift force while retaining the energy consumption. The effect of non-uniform

stiffness distribution was also experimentally studied by Kancharala and Philen.²³ The chordwise-varying stiffness improved both the thrust and propulsion efficiency, which was attributed to the larger bending curvature and trailing edge amplitude.

The material flexibility also raises the possibility of resonance between the actuating motion and the natural frequency of the structure.^{24–26} Kang *et al.*²⁷ numerically studied three flexible wings with chordwise, spanwise, and isotropic flexibility, respectively. They established a correlation between the thrust force and a newly defined maximum relative wing-tip deformation parameter and also stressed that the maximum thrust force was obtained when the wing moved near the resonance frequency while the optimal efficiency was achieved at approximately half of the wing’s natural frequency. By experimentally examining the dynamics of flexible pitching panels with various flexibilities, Dewey *et al.*²⁸ pointed out that resonance alone was insufficient to produce maximum propulsive efficiency and the optimal Strouhal number range should be simultaneously satisfied. Nevertheless, Ramanarivo *et al.*²⁹ argued that flapping wings created the best performance by coordinating the kinematics and the deformation rather than seeking a specific structural resonance condition of the wing. Indeed, certain insects in nature are observed to flap their wings at only a fraction of the resonance frequency.^{30,31} The mechanisms behind the resonance may need further investigation.

For flexible foils, the mass ratio also plays an important role in determining the performance of force generation. The passive structural conformations can be divided into two categories based on the mass ratio of the foil, namely, fluid-driven and inertia-driven deformations.³² Zhu³³ numerically examined the dynamics of a flexible foil in both regimes and concluded that the fluid-induced deformation increases both thrust and propulsion efficiency in a wide range of structural flexibility while the inertia-induced deformation generally deteriorates the performance of the foil. Similar conclusions were also drawn by Olivier and Dumas.³⁴

Despite extensive studies on the dynamics of flexible flapping foils, the bending stiffness of the foil, including both uniform and non-uniform distributions, has been considered a time invariant. With the advent of new smart materials, Young’s modulus of such materials can be controlled by the current intensity.³⁵ These new materials have potential applications in the design of MAVs, which can extend the possible degrees-of-freedom in control. Unfortunately, little attention has been paid to the investigation of relevant topics. Here, we examine the possibility of performance enhancement via time-varying material properties. Specifically, we numerically investigate the dynamics of a two-dimensional flapping foil with time-varying bending stiffness. The objective is to investigate how a time-varying bending stiffness possibly affects the dynamics and propulsion performance of a flapping foil. The novelty of the current work is that the foil’s flexibility is no longer a time-invariant and a better understanding of its effect may contribute to future novel mechanical designs and control strategies of MAVs. To the best knowledge of the authors, the present study would be the first numerical investigation attempting to address the effect of time-dependent bending stiffness on the dynamics of a flexible foil.

The rest of this paper is organized as follows: in Sec. II, the structure and kinematics of the foil are described, and the parameters characterizing the performance are defined. In Sec. III,

the governing equations and numerical methods used in the present fluid-structure interaction (FSI) solver are introduced in brief. In Sec. IV, the numerical results, including the deformation, the force generation, and the near-body flow field are presented. The conclusions are drawn in Sec. V.

II. PROBLEM STATEMENT

In the present study, we numerically examine the propulsion performance of a two-dimensional flapping foil in a uniform flow, as depicted in Fig. 1. The foil has a length L and thickness h ($=0.01L$). Structurally, the foil is modeled as a nonlinear Euler–Bernoulli beam. The dimensionless bending stiffness of the foil is defined as $K \equiv EI/\rho U_\infty^2 L^3$, where E is Young’s modulus, I is the second moment of inertia, ρ is the flow density, and U_∞ is the incoming flow velocity. The mass ratio is defined as $\tilde{m} \equiv \rho_s h/\rho L$, where ρ_s is the structural density. Here, the mass ratio is chosen to be $\tilde{m} = 0.2$.

Kinematically, the leading edge of the foil undergoes a heave motion in the y -direction, which can be described as

$$y_{LE}(t) = a_0 \cos(2\pi ft), \tag{1}$$

where a_0 is the heave amplitude and is chosen to be $a_0 = 0.5L$, f is the motion frequency, and t is the time. The Strouhal number in the present study is defined based on the foil length as $St_c = fL/U_\infty$. Previous biomimetic studies have revealed that the Strouhal numbers of many fish, birds, and insects range from 0.25 to 0.4 and some species are cruising at higher Strouhal numbers up to 0.7.³⁶ Therefore, in the current work, St_c is selected to be 0.5. Different from previous studies on flapping foils, Young’s modulus of the foil in the present work is a time-dependent variable, which is defined as

$$E(t) = E_0 \times 10^{\beta \cos(2\pi ft + \phi)}, \tag{2}$$

where β is a control parameter and ϕ is the phase between the heave motion and the time-varying Young’s modulus. Here, β is fixed at unity. It should be noted that Eq. (2) is defined solely to set a design objective, which is not the stiffness variation of the currently available material. However, it should be noted that with the advance of materials science, there are some available materials whose flexibility can be changed by voltage (e.g., conductive propylene-based elastomers³⁵) or temperature (e.g., low-melting-point-alloys³⁷). Since the variation profiles of temperature or voltage can be arbitrarily designed (especially the voltage), we believe that it is very possible to achieve a stiffness profile satisfying Eq. (2).

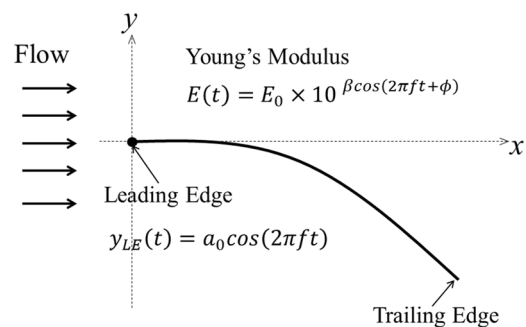


FIG. 1. Sketch of the flapping foil with time-varying bending stiffness.

The propulsion performance of the foil is featured by the mean thrust coefficient \bar{C}_T , the mean lift coefficient \bar{C}_L , the mean power expenditure coefficient \bar{C}_P , and the propulsion efficiency η . These mean values are evaluated by averaging the instantaneous coefficients over one motion period T . The instantaneous thrust coefficient is defined as

$$C_T(t) = \frac{-F_X(t)}{0.5\rho U_\infty^2 L^2}, \quad (3)$$

where $F_X(t)$ is the x -component of the instantaneous hydrodynamic force $\mathbf{F}(t)$.

Similarly, we have

$$\begin{aligned} C_L(t) &= \frac{F_Y(t)}{0.5\rho U_\infty^2 L^2}, \\ C_P(t) &= \frac{P(t)}{0.5\rho U_\infty^3 L^2}, \end{aligned} \quad (4)$$

where $F_Y(t)$ are the components of the instantaneous hydrodynamic force $\mathbf{F}(t)$ in the y direction and $P(t)$ is the instantaneous power expenditure, which is evaluated as

$$P(t) = \iint_S -\mathbf{F}(\mathbf{x}, t) \cdot \mathbf{V}_g(\mathbf{x}, t) d\mathbf{x}, \quad (5)$$

where $\mathbf{V}_g(\mathbf{x}, t)$ is the local moving velocity of the foil. The negative C_P value corresponds to the scenario that energy is transferred from the flow to the foil. However, there is no guarantee that this energy can be stored as elastic energy in the structure and released later. Therefore, we assume that the energy transferred from the fluid to the foil cannot be reused in order to avoid over-estimating the efficiency; thus, the negative values of $C_P(t)$ are set to be zero.^{22,32} Therefore, the propulsion efficiency η is calculated as

$$\eta = \frac{-\bar{F}_X U_\infty}{\bar{P}} = \frac{\bar{C}_T}{\bar{C}_P}. \quad (6)$$

III. MATHEMATICAL FORMULATION AND NUMERICAL METHODS

Two main parts are included in the present fluid-structure interaction solver, namely, a flow solver and a structural solver. In the fluid part, the unsteady compressible Navier–Stokes equations are solved using a finite volume method. The flow governing equations can be expressed in its integral form as follows:

$$\frac{\partial}{\partial t} \iiint_V \mathbf{Q} dV + \iint_{\partial V} \mathbf{G}_c d\mathbf{S} - \iint_{\partial V} \mathbf{G}_v d\mathbf{S} = 0, \quad (7)$$

where $\mathbf{Q} = (\rho, \rho\mathbf{v}, \rho E)^T$ is the conservative variable vector, where ρ is the fluid density, \mathbf{v} is the velocity vector, and E is the total energy, V is the control volume, ∂V is the boundary surface enclosing the volume, \mathbf{S} is the surface vector in the outward direction, and \mathbf{G}_c and \mathbf{G}_v are the convective and diffusive flux vectors, respectively.

The fluid governing equation is discretized by a cell-centred finite volume method based on an overset, multi-block structured grid system.^{38,39} With a structured grid method, the fluid domain is divided into an array of hexahedral cells. Each grid cell is uniquely denoted by three indices i, j, k . For each hexahedral cell (i, j, k) , the

conservation laws are applied, and the following semi-discrete form can be derived:

$$\frac{\partial}{\partial t} (\mathbf{Q}_{i,j,k} \Delta V_{i,j,k}) - \mathbf{F}_{i,j,k} = \mathbf{A}_{i,j,k}, \quad (8)$$

where $\mathbf{F}_{i,j,k}$ is the total convective and diffusive fluxes going through the surface of the hexahedral cell and $\mathbf{A}_{i,j,k}$ denotes the artificial dissipation, which is used for numerical stability.⁴⁰

For unsteady flows, the dual-time stepping algorithm⁴¹ is employed for the temporal integration, where Eq. (8) is reformulated as a steady-state problem with a pseudo-time \tilde{t} ,

$$\frac{\partial}{\partial \tilde{t}} \mathbf{Q}^{n+1} = \frac{1}{\Delta V^{n+1}} \tilde{\mathbf{F}}(\mathbf{Q}^{n+1}), \quad (9)$$

where

$$\begin{aligned} \tilde{\mathbf{F}}(\mathbf{Q}^{n+1}) &= \mathbf{F}(\mathbf{Q}^{n+1}) + \mathbf{A}(\mathbf{Q}^{n+1}) \\ &\quad - \frac{3(\mathbf{Q}\Delta V)^{n+1} - 4(\mathbf{Q}\Delta V)^n + (\mathbf{Q}\Delta V)^{n-1}}{2\Delta t}. \end{aligned} \quad (10)$$

Equation (9) is then integrated using a hybrid multistage Runge–Kutta scheme. At each time step, the domain connectivity needs to be established for interpolation if the overset grid method is used for flow simulation. In the present paper, this is achieved using an implicit hole cutting method.³⁹ It should be noted that the present flow solver is developed for three-dimensional problems. For the two-dimensional problem considered here, two layers of mesh vertices are used to form three-dimensional control volumes, and the two planes in the spanwise direction are considered as symmetric planes.

Structurally, the dynamics of the nonlinear Euler–Bernoulli beam is governed by⁴²

$$\rho_s h \frac{\partial^2 \mathbf{x}}{\partial t^2} + \frac{\partial^2 \mathbf{x}}{\partial s^2} \left(\frac{Eh^3}{12} \frac{\partial^2 \mathbf{x}}{\partial s^2} \right) - \frac{\partial}{\partial s} \left\{ Eh \left[1 - \left(\frac{\partial \mathbf{x}}{\partial s} \cdot \frac{\partial \mathbf{x}}{\partial s} \right)^{-0.5} \right] \frac{\partial \mathbf{x}}{\partial s} \right\} = \mathbf{F}_f, \quad (11)$$

where \mathbf{x} is the instantaneous position of the foil and s ($0 < s < L$) is the Lagrangian coordinate, ρ_s and h are the density and thickness of the foil, respectively, E is Young’s modulus of the foil, and \mathbf{F}_f is the fluid force.

At the basal end ($s = 0$) of the foil, a boundary condition with the prescribed motion is applied,

$$\begin{aligned} \mathbf{x}(0, t) &= \mathbf{x}(0, y_{LE}(t)), \\ \frac{\partial \mathbf{x}(0, t)}{\partial s} &= [1, 0]^T. \end{aligned} \quad (12)$$

At the foil tip ($s = L$), the free boundary condition is employed,

$$\begin{aligned} \frac{\partial \mathbf{x}}{\partial s} \left(\frac{Eh^3}{12} \frac{\partial^2 \mathbf{x}}{\partial s^2} \right) - Eh \left[1 - \left(\frac{\partial \mathbf{x}}{\partial s} \cdot \frac{\partial \mathbf{x}}{\partial s} \right)^{-0.5} \right] \frac{\partial \mathbf{x}}{\partial s} &= 0, \\ \frac{\partial^2 \mathbf{x}}{\partial s^2} &= 0. \end{aligned} \quad (13)$$

Equation (11), together with boundary conditions (12) and (13), is discretized using a second-order finite difference method, and the resulting linear system is solved with an iterative Gauss–Seidel method.^{33,42}

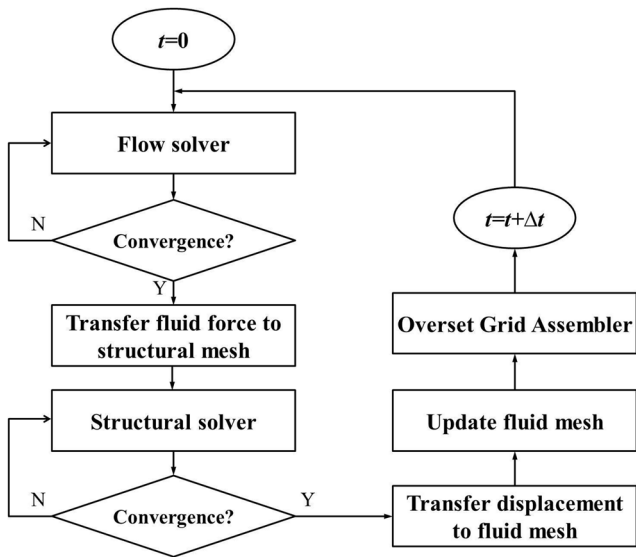


FIG. 2. Coupling procedure of different modules in the present fluid-structure interaction solver.

In the present fluid-structure interaction solver, the flow model is coupled with the structural model using a partitioned approach known as the conventional serial staggered procedure.⁴³ As shown in Fig. 2, in the present coupling method, the flow solver and the structural solver exchange data only once within one time step, which are categorized into explicit schemes. Due to the inconsistency between the fluid mesh and structural mesh, interpolations of fluid forces and structural displacements must be performed at the fluid-structure interface. For the force interpolation, as demonstrated in Fig. 3(a), both the fluid grid nodes on the surface of the foil and the structural grid nodes are first projected to a common planar plane, on which a bilinear (linear for two-dimensional problems) interpolation is then performed.³⁸ The structural displacements are transferred to the fluid mesh by a constant volume tetrahedron method.⁴⁴ As illustrated in Fig. 3(b), each node q_f on the fluid grid is connected rigidly to three closest points $q_{s,i}$ on the solid plane spanning a tetrahedron. During the deforming process, the volume of the tetrahedron is assumed to be a constant. The out-of-plane distance $\|\gamma\vec{d}\|$ thus

becomes a function of the in-plane stretching of the three connected solid points. In the local coordinate system spanned by difference vectors \vec{a} and \vec{b} and the normal vector $\vec{c} = \vec{a} \times \vec{b}$, the position of the fluid node q_f can be described as

$$q_f - q_{s,1} = \alpha\vec{a} + \beta\vec{b} + \gamma\vec{d}. \tag{14}$$

After the deformation of the structural grid, the vectors \vec{a} , \vec{b} , and, thus, \vec{d} are known. The parameters α and β are chosen to be constant, i.e., $\alpha = \alpha_0$ and $\beta = \beta_0$ (the subscript 0 denotes the initial values). The parameter γ is defined as

$$\gamma = \frac{\vec{d}_0 \cdot \vec{d}_0}{\vec{d} \cdot \vec{d}} \gamma_0, \tag{15}$$

which ensures the volume of the tetrahedron spanned by \vec{a} , \vec{b} , and \vec{c} to be a constant.⁴⁴

IV. RESULTS

The problem depicted in Fig. 1 is solved using the fluid-structure interaction solver described in Sec. III. The computational domain and corresponding boundary conditions are demonstrated in Fig. 4(a). A non-reflective far-field boundary condition is applied at the outer boundaries of the computational domain while a no-slip boundary condition is used at the surface of the foil. The overset grids used for flow simulation are shown in Fig. 4(b). The Reynolds number based on the length of the foil is $Re = 1000$. In relatively low Reynolds number regimes (below or in the order of 10^3), turbulence may have a subtle effect on the flow dynamics. For these scenarios, laminar flow models are usually used for biomimetic problems (see examples in Refs. 45 and 46). Therefore, the flow in the present study is assumed to be laminar. The current compressible flow solver has been extensively validated in our previous work,^{47,48} and the present FSI solver has also been validated via several benchmarks,³⁸ all the results showed good agreement with those from the literature.

In the present paper, two different foils are examined. In the first case (hereafter referred to as foil A), the foil has a constant flexibility, i.e., the bending stiffness does not change with time $E(t) = E_0$. In the second case (foil B), the bending stiffness of the foil is time-dependent, i.e., the performance of the foil is not only affected by E_0 but also determined by parameters ϕ in Eq. (2). To have a fair comparison between foil A and foil B, the flexibility of the foil will

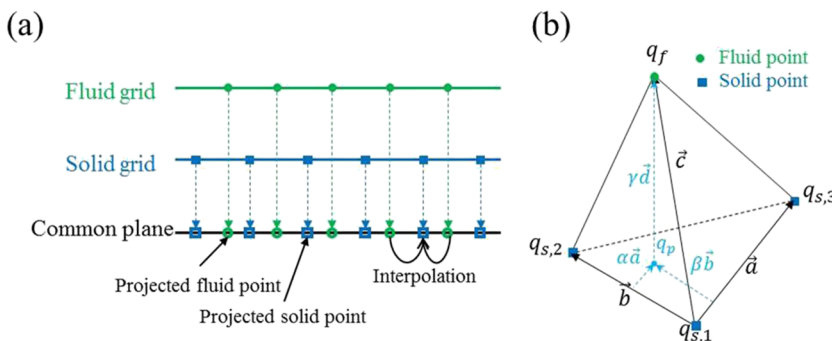


FIG. 3. (a) Projection-based flow force interpolation, and (b) the constant-volume tetrahedron method for structural displacement transfer.

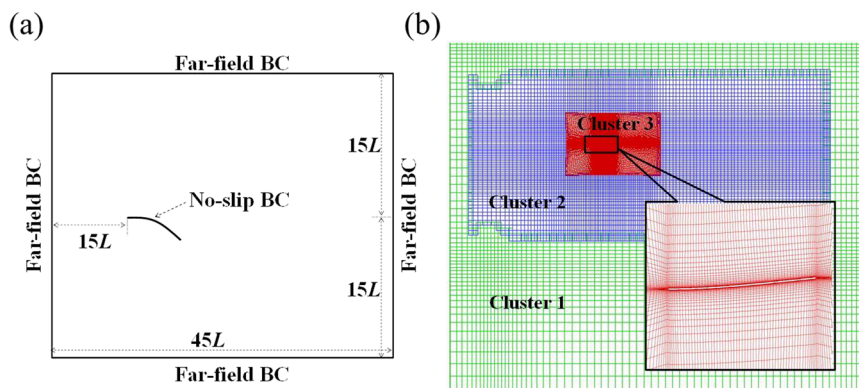


FIG. 4. (a) Computational domain and (b) fluid mesh for the proposed problem.

be depicted by the time-averaged normalized bending stiffness \bar{K} , which is defined as $\bar{K} = \int_t^{t+T} E(t)I/\rho U_\infty^2 L^3 dt$.

In addition, a self-consistency study is carried out to justify the fluid mesh, physical time step, and number of solid nodes along the foil used here. To check the sensitivity to the fluid mesh, three meshes with different densities, namely, mesh_F (fine mesh), mesh_M (medium mesh), and mesh_C (coarse mesh) are generated. More details about the meshes can be found in Table I. Similarly, three physical time steps ($dt = T/160$, $T/200$, and $T/240$) and three numbers of structural grid points along the foil ($N_p = 81$, 101, and 121) are chosen for this sensitivity study. Figures 5(a)–5(c) demonstrate the sensitivity of the present code to the fluid mesh density, time step size, and number of solid nodes along the foil, and the time-averaged values are summarized in Table II. It is seen that with sufficiently high fluid/structural mesh densities and a sufficiently small time step, the results are not sensitive to these numerical parameters. On the basis of the self-consistency study, the simulations in the following paper are based on mesh_M, $dt = T/200$, and $N_p = 101$.

A. Force generation and propulsion efficiency

The time-averaged thrust, lift coefficient, and propulsion efficiency as functions of the mean bending stiffness of foils A and B are shown in Fig. 6. It is observed that for the foil with constant stiffness (foil A), \bar{C}_T and η increase as the flexibility increases and then decline significantly after reaching a peak. This is consistent with the general conclusion from previous studies on flexible flapping foils^{18,21} that the propulsion performance of a flapping foil can be enhanced by a certain amount of flexibility but will be undermined if the flexibility is excessive. The force creation of the

flexible flapping foil is significantly influenced by making the bending stiffness of the foil a time-dependent variable (foil B). Specifically, the time-averaged thrust coefficients of foil B at $\phi = 0^\circ$ are substantially larger than those of foil A for higher \bar{K} values whereas the \bar{C}_T peaks of foil B at $\phi = 60^\circ$ and 90° are lower than those of foil A, as shown in Fig. 6(a). The maximum thrust coefficient generated by foil B at $\phi = 0$ is created at higher rigidity and is $\sim 52\%$ higher than that of foil A. In addition, foil B produces considerable net lift force at all ϕ values, as demonstrated in Fig. 6(b), while the time-averaged lift force of foil A is almost zero. The largest lift force is created by foil B at $\phi = 90$. This actually provides an alternative approach of creating lift force with symmetric sinusoidal kinematics. As illustrated in Fig. 6(c), foil B achieves higher propulsion efficiency at $\phi = 0^\circ$ than at other ϕ values. Besides, foil B also produces higher propulsion efficiency than foil A at larger bending stiffness at $\phi = 0^\circ$. Despite this, its peak value still does not surpass that of foil A. However, this is still of importance in situations where the size of the wing is strictly restricted.

Figure 7 shows the variations in \bar{C}_T , \bar{C}_L , and η of foil B as functions of phase ϕ at different mean flexibilities. In general, both \bar{C}_T and η decrease as the phase ϕ increases at first and then start to increase after reaching the minimum values. In terms of thrust generation and propulsion efficiency, the best performance is accomplished at $\phi = 0^\circ$ and 180° . Although the poorest performance is achieved when ϕ is in the range of 90° – 120° , the foil produces the largest magnitude of lift force in that range.

Figures 8(a) and 8(c) demonstrate the instantaneous thrust coefficient in one motion period at $\bar{K} = 1.42$ and 2.84, respectively. It is seen that foil A produces two identical C_T peaks during the downstroke and the upstroke periods.²⁷ Compared with foil A, foil B at $\phi = 0^\circ$ yields a lower thrust peak value during the downstroke but a significantly higher peak during the upstroke, which leads to a larger time-averaged thrust force. On the contrary, at $\phi = 90^\circ$, foil B barely creates net thrust during the downstroke, leading to a decrease in time-averaged thrust. The time history of the lift coefficient is shown in Figs. 8(b) and 8(d), from which we can observe that foil A generates the same amount of lift force during the downstroke and the upstroke but in opposite directions, i.e., the time-averaged lift force for foil A is almost zero. As plotted in Fig. 6(b), foil B creates considerable net lift force at both $\phi = 0^\circ$ and 90° , which is attributed to the larger lift force produced during the upstroke.

TABLE I. Grid cell numbers and first layer thickness for three different meshes.

	Cluster 1	Cluster 2	Cluster 3	Total	First-layer thickness (L)
Mesh_C	7 350	8 400	6 300	22 050	0.001
Mesh_M	9 600	11 200	11 200	32 000	0.001
Mesh_F	12 150	13 500	20 350	46 000	0.001

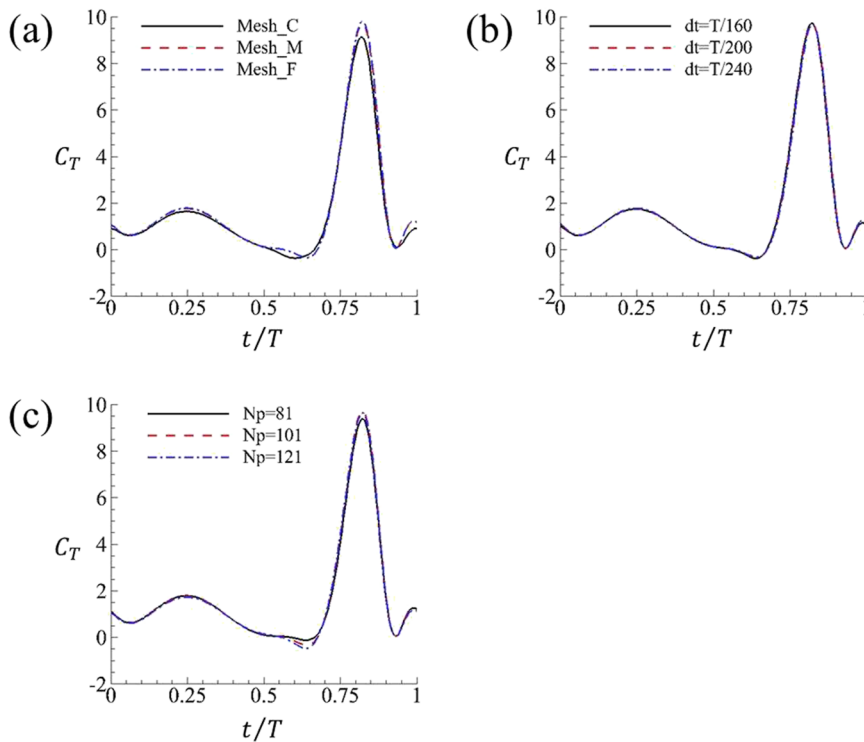


FIG. 5. Sensitivity study of the present code to the (a) CFD mesh density ($dt = T/200$ and $N_p = 101$), (b) time step size (mesh_M and $N_p = 101$), and (c) number of structural nodes along the foil (mesh_M and $dt = T/200$). The plots show the instantaneous thrust coefficient of foil B (time-varying stiffness) at $St_c = 0.5$, $\bar{K} = 2.84$, and $\phi = 0^\circ$.

Figure 9 demonstrates the instantaneous thrust and lift coefficients in long time spans and the corresponding power spectra. It is observed from Figs. 9(a) and 9(c) that the variations in both thrust and lift coefficients become periodical after 10 flapping cycles. The power spectrum of the thrust [Fig. 9(b)] shows one dominant component ($\hat{f}/f = 2$, where \hat{f} is the frequency of the fluid force) and three other considerable components ($\hat{f}/f = 1, 3$, and 4). Similarly, the spectrum of the lift force [Fig. 9(d)] also includes multiple considerable frequency components. However, it has two dominant frequencies ($\hat{f}/f = 1$ and 2) and two other considerable components ($\hat{f}/f = 3$ and 4).

B. Foil deformations

Figure 10 demonstrates the deformation patterns and trailing edge trajectories of foil A and foil B at $\phi = 0^\circ$ and 90° . It is seen

TABLE II. Summary of the time-averaged thrust coefficients from various mesh densities and a number of structural points and time steps.

	N_p	dt/T	\bar{C}_T	Difference (%)
Mesh_F	101	1/200	1.788	0.00
Mesh_C	101	1/200	1.651	-7.68
Mesh_M	101	1/200	1.770	-1.01
Mesh_M	101	1/160	1.767	-1.19
Mesh_M	101	1/240	1.770	-0.99
Mesh_M	81	1/200	1.743	-2.52
Mesh_M	121	1/200	1.743	-2.50

that for all cases, only the first bending mode is excited. For foil A, the deformation pattern is symmetrical about the y-axis, and the trailing edge trajectory has a symmetrical “figure-eight” shape. However, this symmetry is broken for foil B. Specifically, foil B creates larger deformation during the upstroke at $\phi = 0^\circ$ while it generates higher conformation during the downstroke at $\phi = 90^\circ$. In addition, the “figure-eight” shapes of the trailing edge trajectory are distorted.

Figure 11 shows the displacements of the leading edge (y_L/a_0) and the trailing edge (y_T/a_0) and the relative deformation ($(y_L - y_T)/a_0$) for foil A and foil B at $\phi = 0^\circ$ and 90° . For all cases, the leading edge of the foil moves sinusoidally, as described in Eq. (1). It is observed that the trailing edge displacement and the relative deformation of foil A also follow a sinusoidal fashion while those of foil B vary with time in a non-sinusoidal manner. Specifically, foil B experiences a surge in relative deformation during the upstroke at $\phi = 0^\circ$ while the largest deformation occurs during the downstroke when $\phi = 90^\circ$.

It can be observed from Fig. 11(a) that the phase lag (θ) between the leading edge motion and the relative deformation for foil A is $\sim 90^\circ$, which agrees with previous studies on the condition that maximizes the thrust force of flexible flapping foils.^{21,27} However, the parameter θ is difficult to be defined for foil B as the variations in the relative deformation are significantly different during the downstroke and the upstroke periods. A comparison between Figs. 11(a) and 8(a) also reveals that foil A creates the largest relative deformation at the instants ($t/T = 0.25$ and 0.75) corresponding to the C_T peaks. Nevertheless, the relationship between the deformation and the force creation becomes more complicated for foil B. At $\phi = 0^\circ$, foil B creates the largest deformation at $t/T = 0.75$ while the thrust

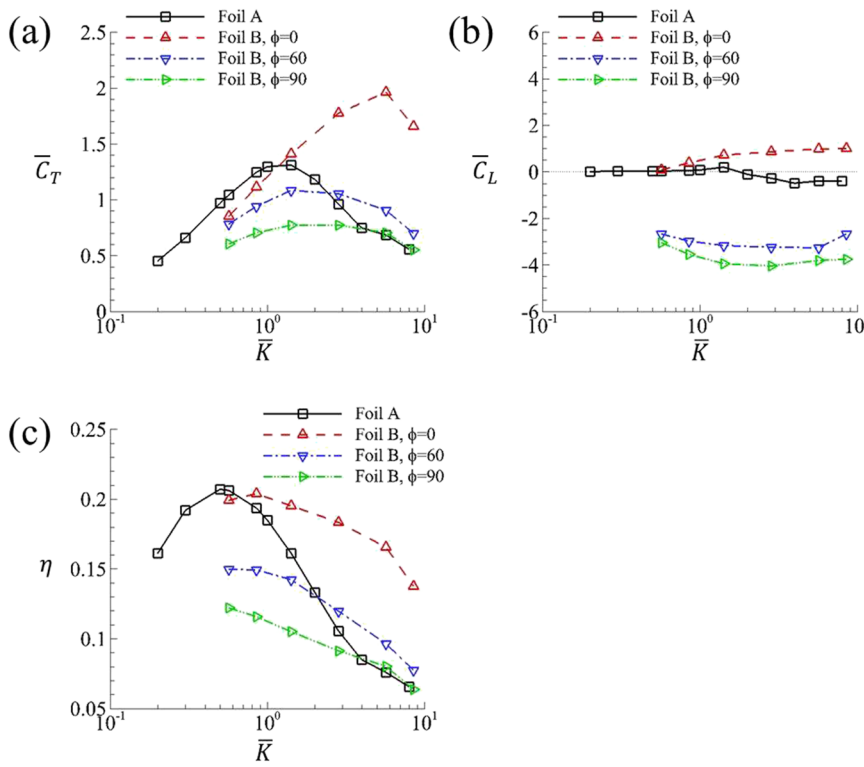


FIG. 6. (a) Time-averaged thrust coefficient \bar{C}_T , (b) the lift coefficient \bar{C}_L , and (c) the propulsion efficiency η as functions of dimensionless averaged bending stiffness \bar{K} for various foils. $St_c = 0.5$. Foil A has constant stiffness; foil B has time-varying stiffness.

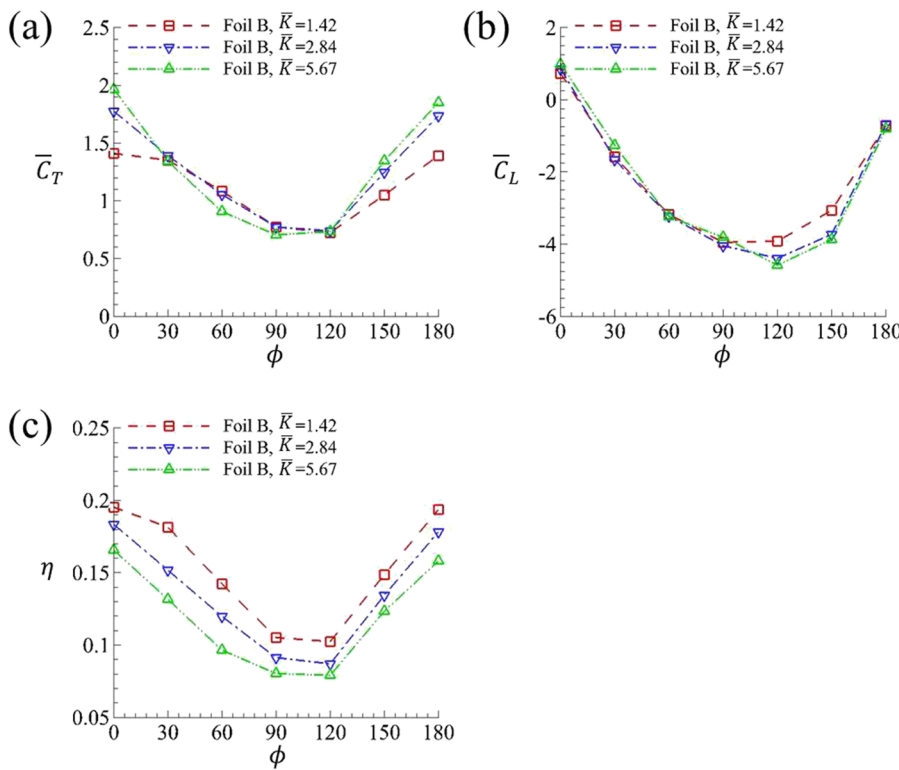


FIG. 7. (a) Time-averaged thrust coefficient \bar{C}_T , (b) the lift coefficient \bar{C}_L , and (c) the propulsion efficiency η as functions of phase ϕ for foil B at different mean flexibilities. $St_c = 0.5$. Foil A has constant stiffness; foil B has time-varying stiffness.

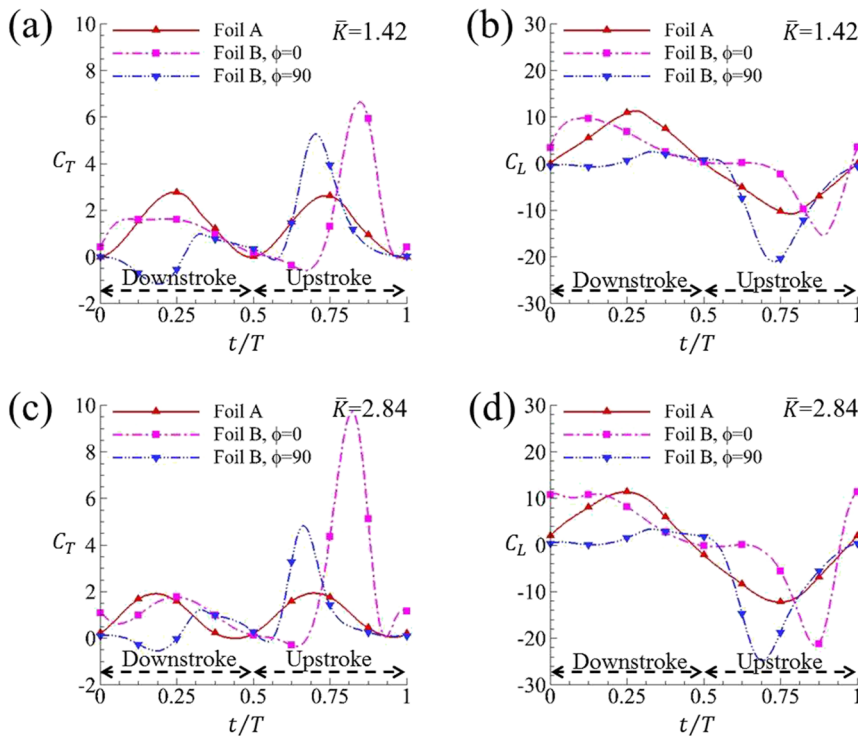


FIG. 8. Time histories of thrust and lift coefficients for foil A (constant stiffness) and foil B (time-varying stiffness): (a) and (b) $\bar{K} = 1.42$ and (c) and (d) $\bar{K} = 2.84$. $St_c = 0.5$.

peak is accomplished at a later time instant, as shown in Fig. 8(a). In contrast, at $\phi = 90^\circ$, the largest relative deformation is generated at $t/T = 0.25$ whereas almost no thrust force is created at this instant.

Figure 12 demonstrates the normalized trailing edge amplitude $A^* = \max(|y_T|/a_0)$ and the maximum relative deformation $Y^* = \max(|y_L - y_T|/a_0)$ of foils A and B. Obviously, foil A has the same tip amplitude and maximum relative deformation during the downstroke and the upstroke. In general, foil A and foil B share some similar variation trends, that is, the tip amplitude increases

as the flexibility increases and then declines after reaching a peak, and the maximum relative deformation increases monotonously as the bending stiffness decreases. Nevertheless, foil B generates significantly different tip amplitudes and maximum relative deformations at the downstroke and the upstroke. Specifically, the largest tip amplitudes and relative deformations at the downstroke [Figs. 12(a) and 12(c)] and the upstroke [Figs. 12(b) and 12(d)] are accomplished at $\phi = 90^\circ$ and $\phi = 0^\circ$, respectively. A closer inspection of Fig. 12 demonstrates that the maximum values of tip amplitude and relative deformation achieved by foil B at $\phi = 90^\circ$ and 0° are similar to each

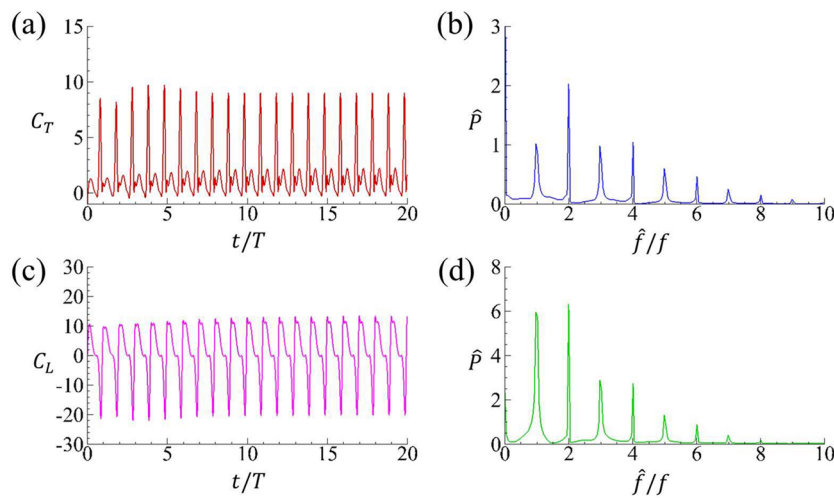


FIG. 9. Time histories and power spectra of the thrust coefficient [(a) and (b)] and the lift coefficient [(c) and (d)] for foil B (time-varying stiffness) at $\bar{K} = 2.84$, $St_c = 0.5$, and $\phi = 0^\circ$. In subplots [(b) and (d)], the frequency is normalized by the heave frequency of the leading edge.

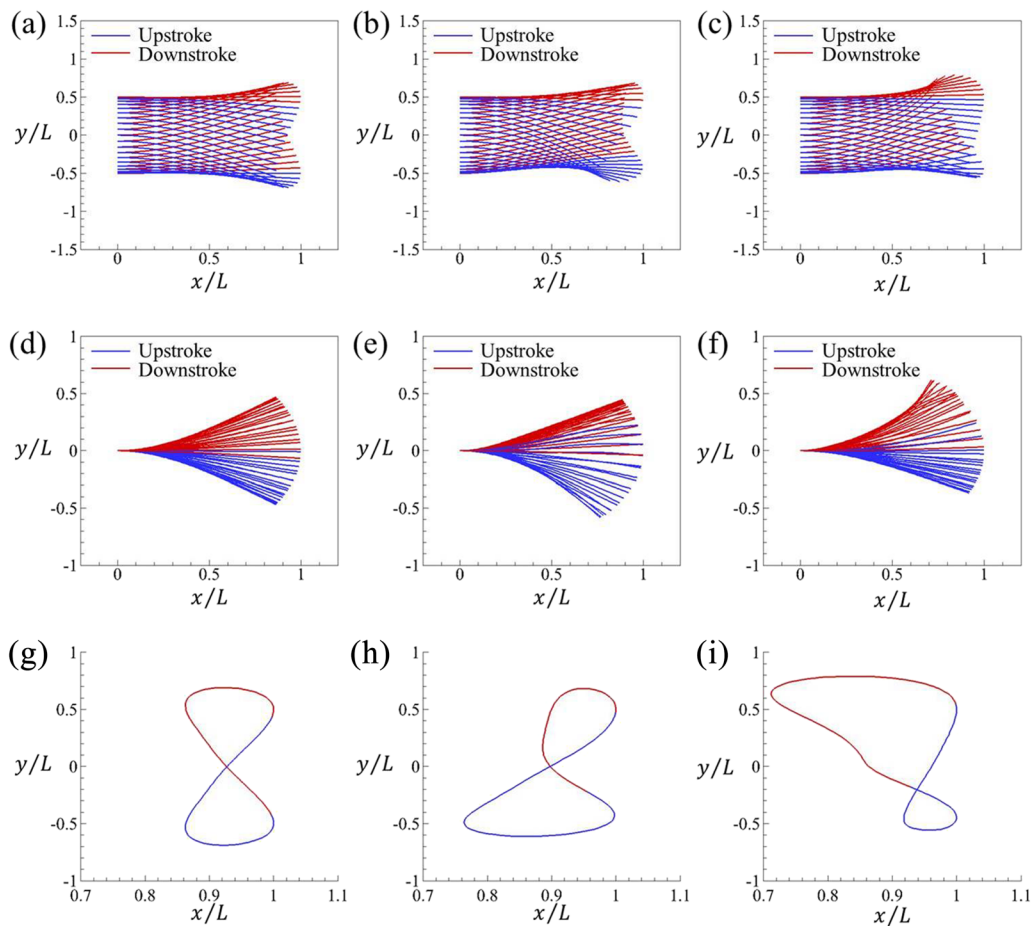


FIG. 10. Deformation patterns and the trailing edge trajectories of the foil: (a), (d), and (g) foil A; (b), (e), and (h) foil B, $\phi = 0^\circ$; and (c), (f), and (i) foil B, $\phi = 90^\circ$. $St_c = 0.5$, $\beta = 1.0$, and $\bar{K} = 0.57$. Subplots [(d)–(f)] show the same deformations as [(a)–(c)] with the leading edges clamped. Foil A has constant stiffness; foil B has time-varying stiffness.

other. However, it is interesting to observe that the high amplitudes and relative deformations created by foil B at $\phi = 90^\circ$ do not contribute much to the thrust generation, as demonstrated in Figs. 6(a) and 8(a). This may be associated with the flow field created by the foil, which will be discussed later.

C. Near-body flow fields

Figures 13–15 demonstrate the vorticity contours within a motion period for foil A and foil B at $\phi = 0^\circ$ and 90° , respectively. It is observed from Fig. 13 that foil A produces a clockwise and a counter-clockwise trailing edge vortex (TEV) during upstroke and downstroke, respectively. These vortices are shed into the wake alternatively, forming a reversed von Karman vortex street, which is known as a thrust-productive wake pattern.¹² However, the wake patterns produced by foil B are very different from that of foil A. Foil B creates a deflected vortex-pair within one motion cycle at $\phi = 0^\circ$, which resembles the deflected wake previously observed from both rigid and flexible flapping foils at higher motion frequencies.^{14,21} The deflected vortex shedding will lead to the generation of finite lift

force, as illustrated in Fig. 6(b), which has also been demonstrated in previous experiments.³ Interestingly, foil B also generates deflected vortex-pairs at $\phi = 90^\circ$, which are distinct from those at $\phi = 0^\circ$. Specifically, for foil B at $\phi = 0^\circ$, the vortex-pair starts to form during the downstroke ($t = T/8$ in Fig. 14) while the vortex-pair is formed at the beginning of the upstroke when ϕ is 0° ($t = 4T/8$ in Fig. 15). Another distinction is that the vortex-pair shed by foil B at $\phi = 0^\circ$ has an “up-down” structure whereas a “fore-rear” arrangement is observed in the wake of foil B at $\phi = 90^\circ$.

The pressure contours and distributions of foil A within one motion period are demonstrated in Fig. 16. The largest pressure difference between the two sides of the foil is accomplished at $t = 2T/8$ and $6T/8$, which correspond to the time instants when the largest deformations are achieved, as shown in Fig. 11(a). The simultaneous creation of the highest pressure difference and relative deformation leads to the generation of thrust peaks shown in Fig. 8(a).

Figure 17 illustrates the same plots as those in Fig. 16 for foil B at $\phi = 0^\circ$. We can observe that the pressure distributions generated by foil B are significantly different from those by foil A. At

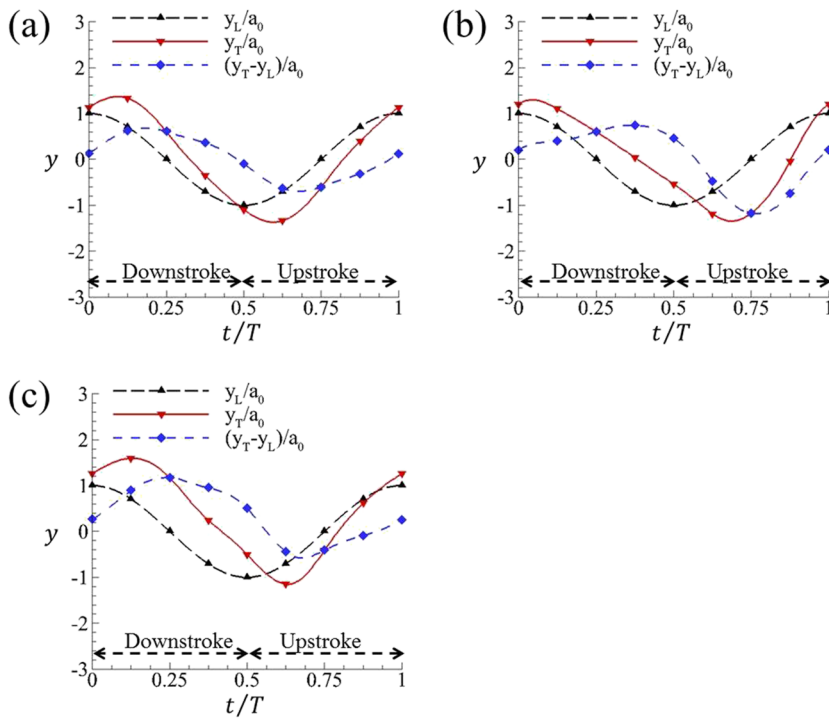


FIG. 11. Normalized leading edge displacement (y_L/a_0), normalized trailing edge displacement (y_T/a_0), and normalized relative deformation $[(y_T - y_L)/a_0]$ as functions of time: (a) foil A, $\phi = 0^\circ$; and (c) foil B, $\phi = 90^\circ$. $St_c = 0.5$, $\beta = 1.0$, and $\bar{K} = 1.42$. Foil A has constant stiffness; foil B has time-varying stiffness.

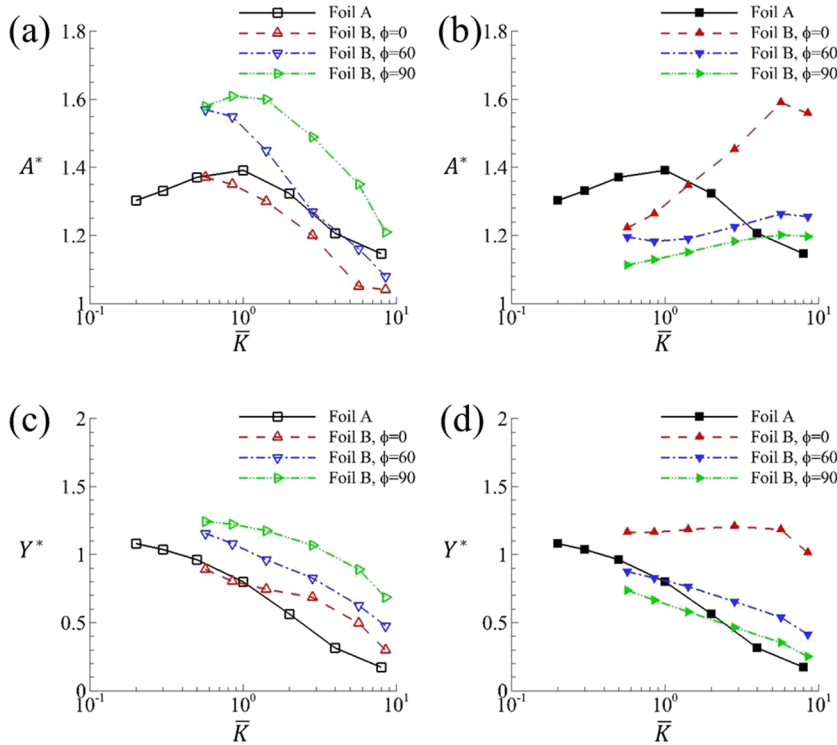


FIG. 12. Normalized tip amplitude (A^*) and maximum relative deformation (Y^*) as functions of dimensionless averaged bending stiffness for foils A and B at (a) and (c) the downstroke and (b) and (d) the upstroke. $St_c = 0.5$ and $\beta = 1.0$. Foil A has constant stiffness; foil B has time-varying stiffness.

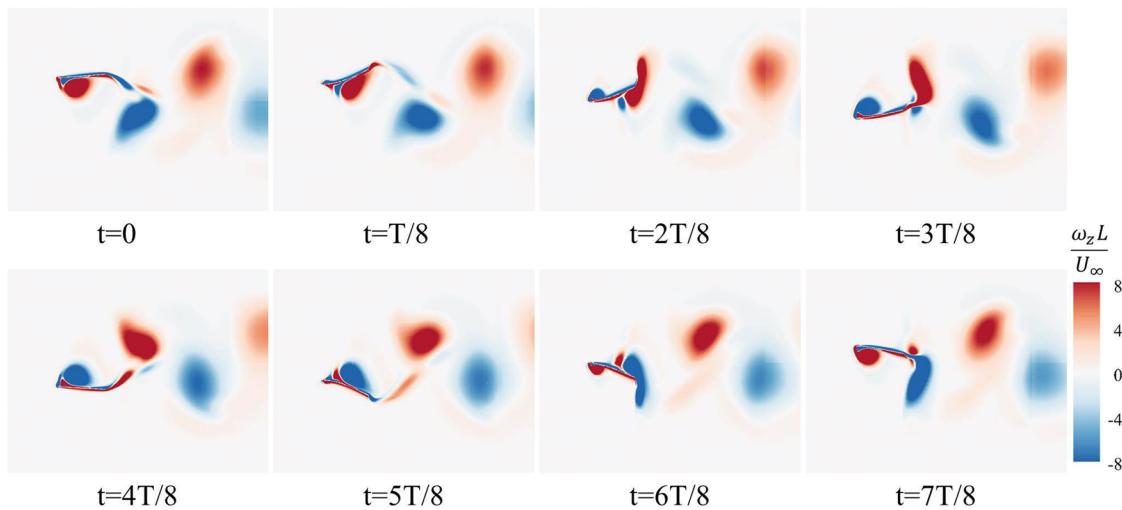


FIG. 13. Instantaneous flow vorticity fields of foil A (constant stiffness) in a motion period. $St_c = 0.5$ and $\bar{K} = 1.42$.

$\phi = 0$, foil B creates high pressure difference at the beginning of the downstroke. However, the large resultant pressure difference only contributes a minor portion to the creation of thrust force due to the small deformation [see Fig. 11(b)], leading to a relatively lower thrust peak during the downstroke, as shown in Fig. 8(a). During the upstroke, the largest deformation and the highest pressure difference are achieved at $t = 6T/8$ and $t = 7T/8$, respectively. As the thrust force is determined by both the magnitude of the pressure difference and the relative deformation orienting it in the thrust direction, the maximum thrust force is accomplished at an instant between $t = 6T/8$ and $t = 7T/8$ [see Fig. 8(a)], indicating an optimal combination of the pressure distribution and the deformation of the foil.

As shown in Fig. 18, foil B at $\phi = 90^\circ$ generates large deformation [see Fig. 11(c)] but little pressure difference during the downstroke. On the contrary, high pressure difference is created at $t = 5T/8$ and $6T/8$ during the upstroke. However, only medium deformations are generated. Therefore, at $\phi = 90^\circ$, foil B creates little thrust during the downstroke, and the maximum value achieved during the upstroke is lower than that at $\phi = 0^\circ$, as shown in Fig. 8(a). The present results highlight the importance of the exact conformation pattern of the foil, which may completely change the flow field and pressure distribution. This is reminiscent of previous studies arguing that flapping wings may manipulate the aerodynamics to produce high performance rather than pursuing the resonance

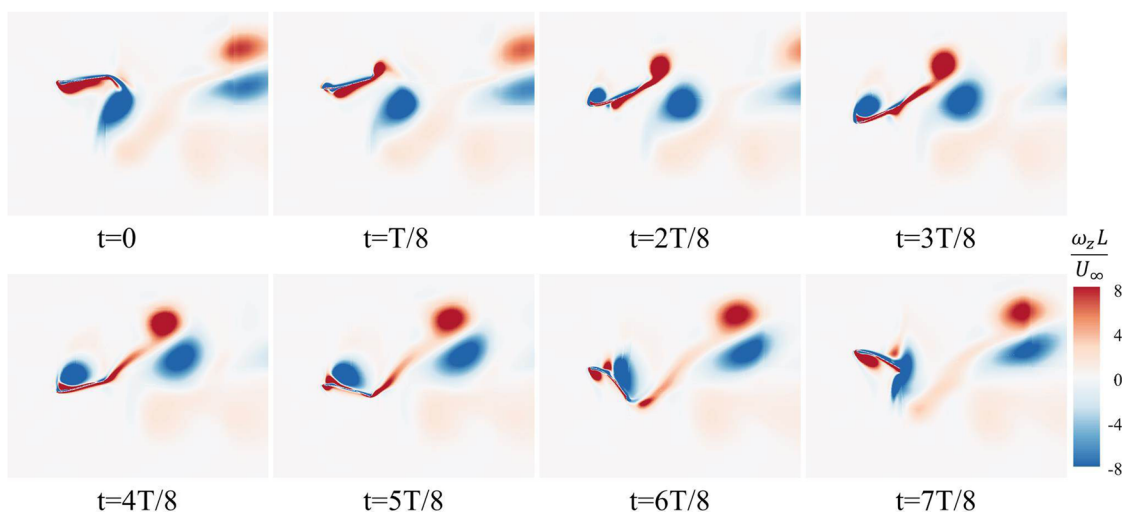


FIG. 14. Instantaneous flow vorticity fields of foil B (time-varying stiffness) in a motion period. $St_c = 0.5$, $\beta = 1.0$, $\bar{K} = 1.42$, and $\phi = 0^\circ$.

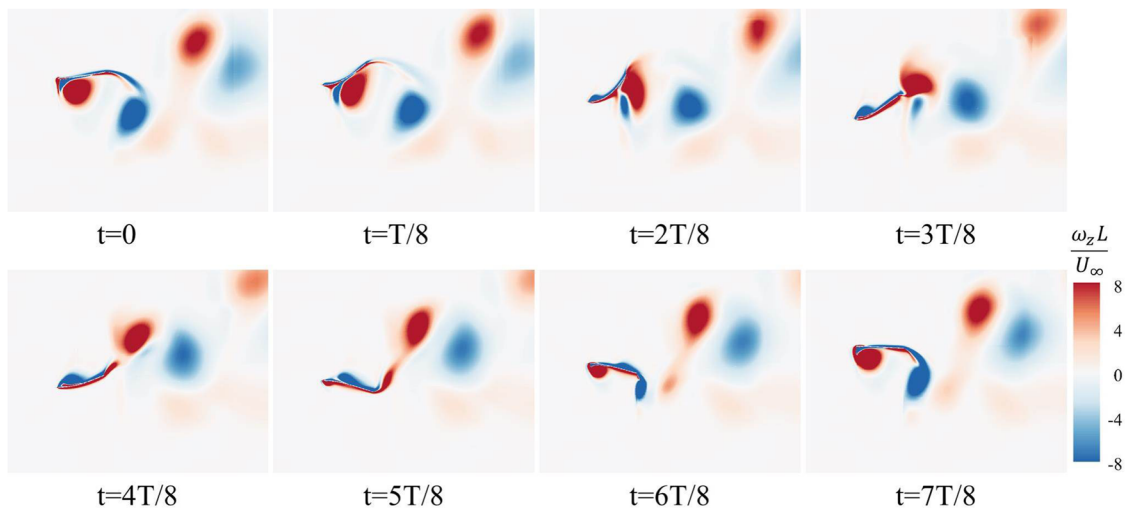


FIG. 15. Instantaneous flow vorticity fields of foil B (time-varying stiffness) in a motion period. $St_c = 0.5$, $\beta = 1.0$, $\bar{K} = 1.42$, and $\phi = 90^\circ$.

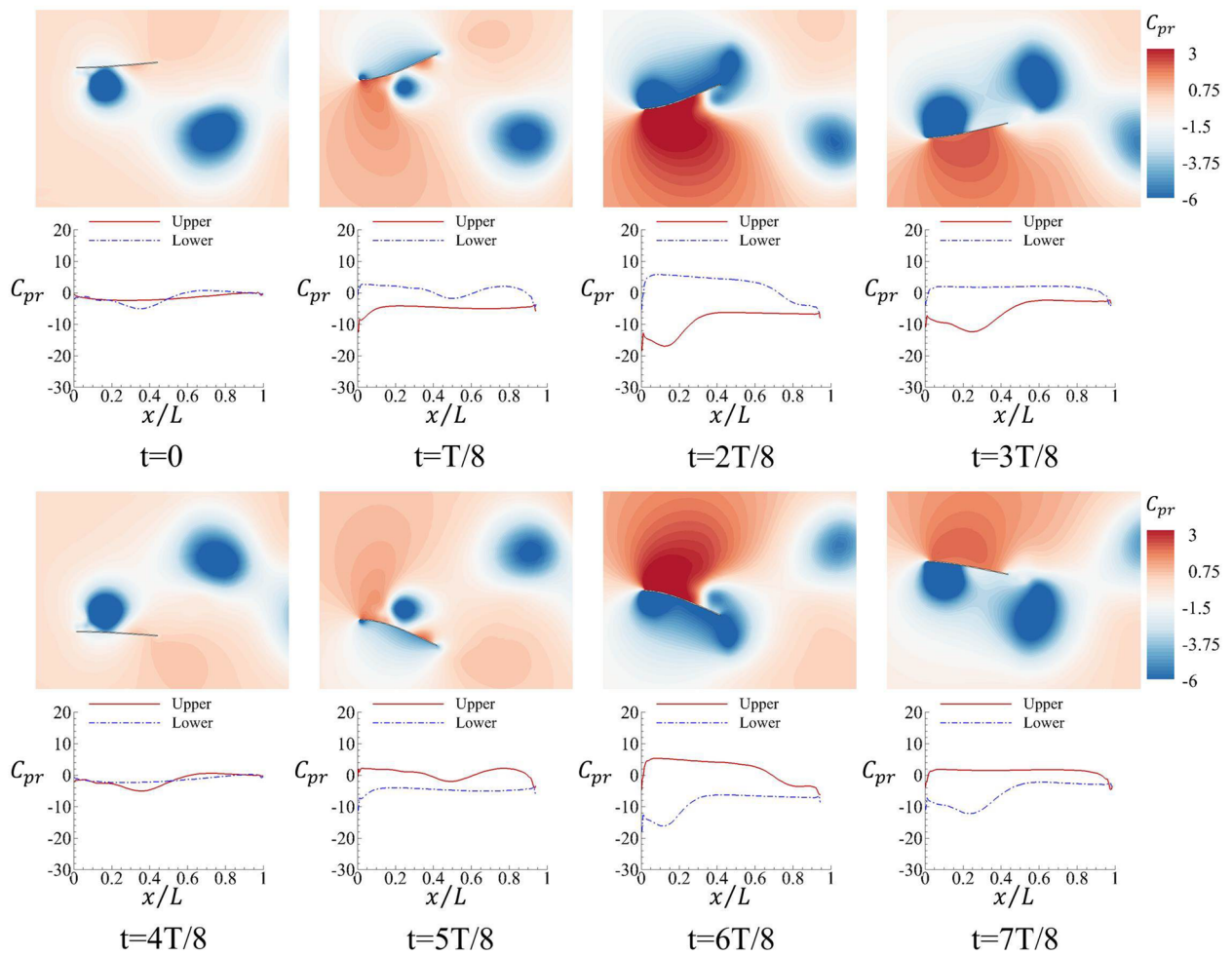


FIG. 16. Instantaneous pressure fields and corresponding pressure coefficient distributions of foil A (constant stiffness) in a motion period. $St_c = 0.5$ and $\bar{K} = 1.42$.

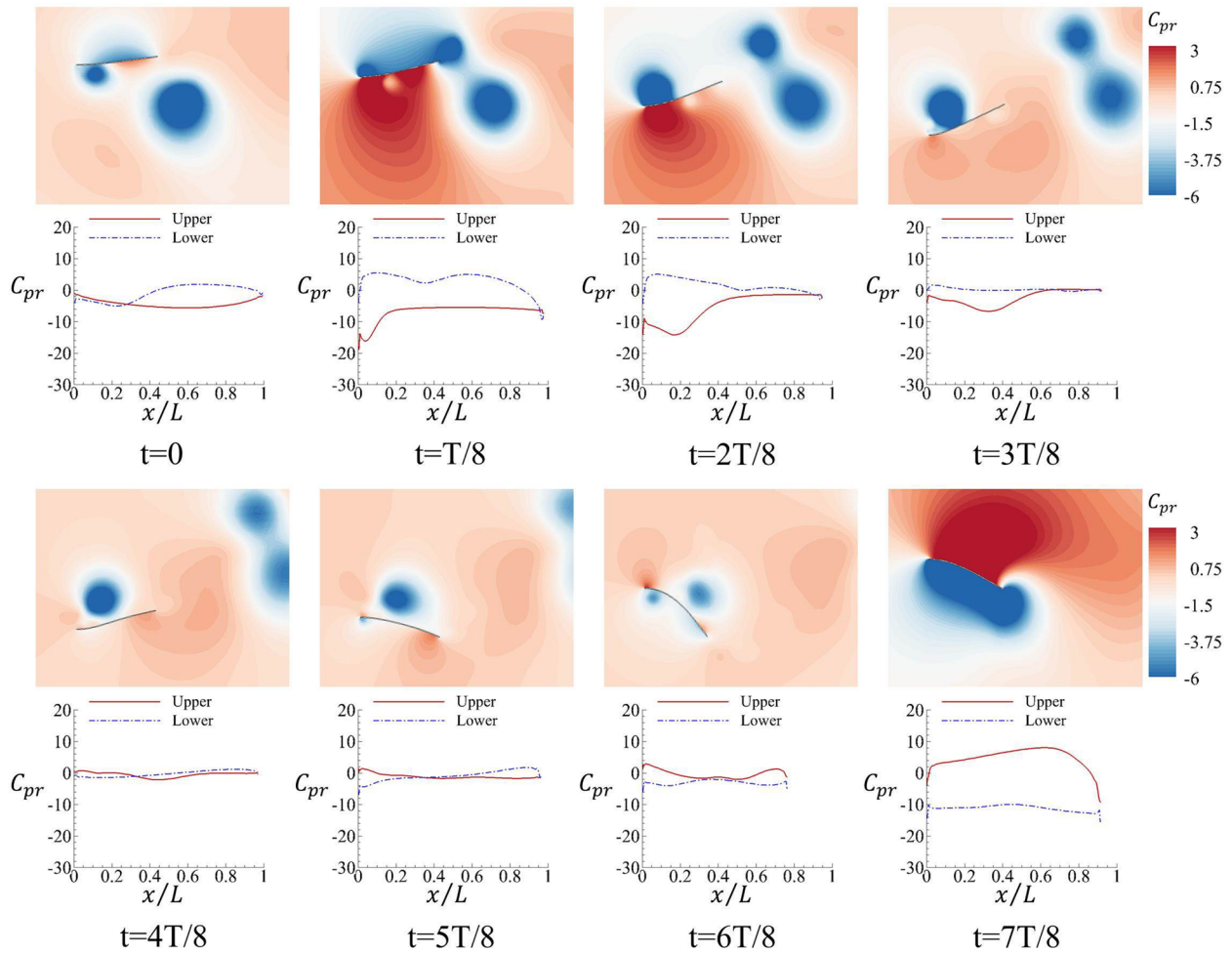


FIG. 17. Instantaneous pressure fields and corresponding pressure coefficient distributions of foil B (time-varying stiffness) in a motion period. $St_c = 0.5$, $\beta = 1.0$, $\bar{K} = 1.42$, and $\phi = 0^\circ$.

condition.²⁹ Indeed, birds and insects may sense the pressure changes around the wing and instantaneously adjust the kinematics to fully exploit the flow energy.

D. Considerations on added mass effect

The thrust generation mechanisms of flight and swimming animals can be generally classified into (1) the added-mass mechanism, and (2) the lift-based mechanism. For the first mechanism, the thrust is created by the reaction force from the accelerated fluid adjacent to the body whereas in the second mechanism, the thrust force is generated by reorienting the lift force due to vortex shedding and body-wake interaction in the moving direction.⁴⁹ To clarify which mechanism is dominant in the thrust production of the present case, the thrust and lift forces due to added mass are evaluated in the current section. However, a direct estimation of the added mass force for a flexible flapping foil in a

viscous flow is extremely difficult;⁵⁰ we, therefore, estimate the added mass force in the present study by simplifying the flexible foil as a rigid one by connecting its leading and trailing points, as demonstrated in Fig. 19(a). The rigid foil undergoes combined heave and pitch motions, where the heave motion still follows a sinusoidal function while the instantaneous pitch angle is calculated from the passive deformation of the foil at the corresponding instant.

Figure 19(b) illustrates the acceleration vectors acting on the center of mass of the simplified rigid foil, where a_h and a_p are accelerations due to heave and pitch motions, respectively. By transforming a_h from the global coordinate system to the body-fixed coordinate system, the normal (F_{an}) and tangential (F_{at}) components of the added mass force can be written as⁵¹

$$\begin{aligned} F_{an} &= -C_{an}\rho V_{rep}a_n, \\ F_{at} &= -C_{at}\rho V_{rep}a_t, \end{aligned} \tag{16}$$

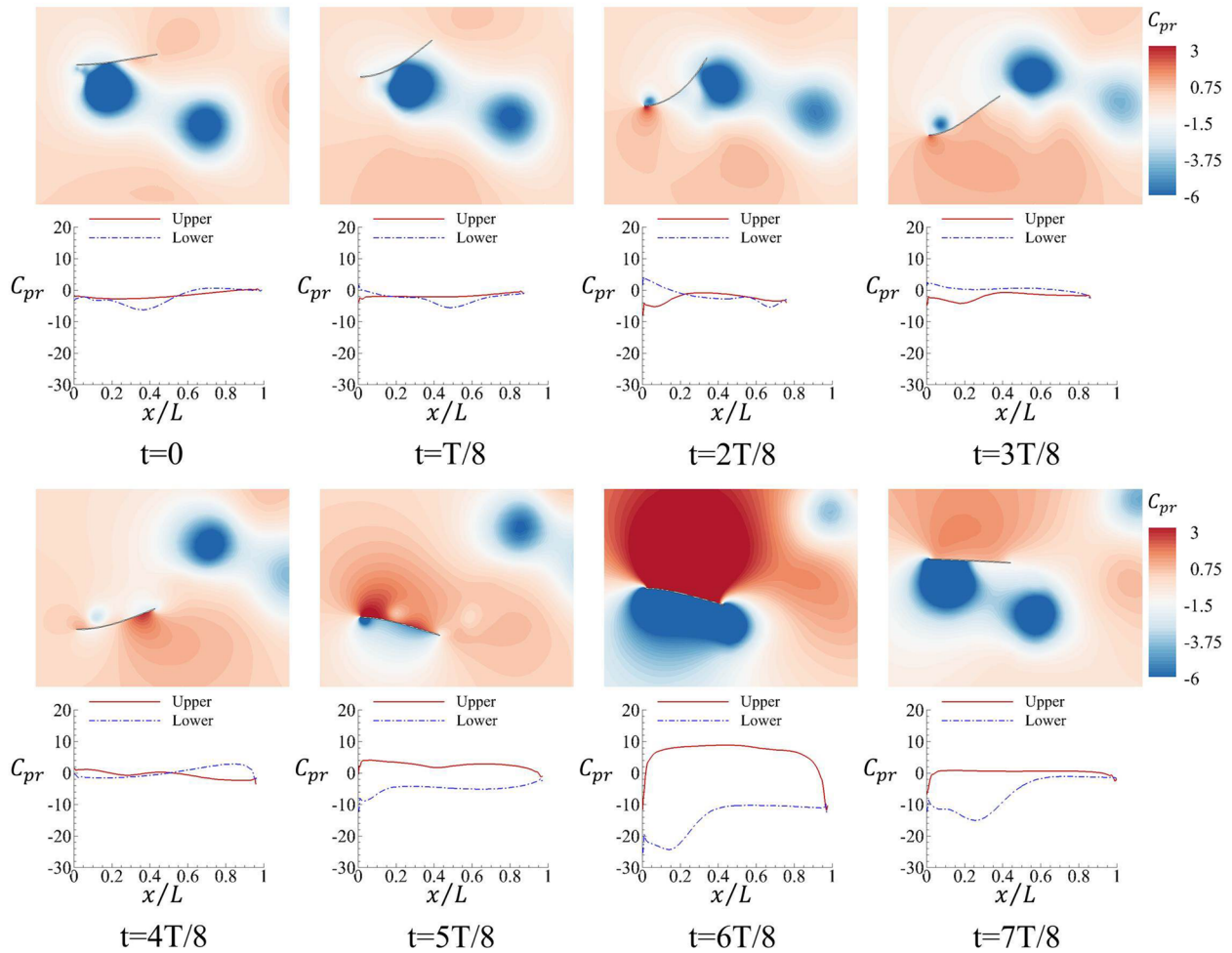


FIG. 18. Instantaneous pressure fields and corresponding pressure coefficient distributions of foil B (time-varying stiffness) in a motion period. $St_c = 0.5$, $\beta = 1.0$, $\bar{K} = 1.42$, and $\phi = 90^\circ$.

where C_{an} (a_n) and C_{at} (a_t) are the added mass coefficients (accelerations) in the normal and tangential directions in the body-fixed system, respectively, and V_{rep} is the representative volume of the fluid, which can be formulated as the volume of a cylinder whose diameter and length are equal to the chordwise and spanwise lengths

of the foil, i.e., $V_{rep} = \pi L^3/4$.^{52–54} For a very thin plate, the tangential component of the added mass coefficient can be approximated as zero ($C_{at} = 0$). Thus, only the added mass force normal to the foil contributes to the total force acting on the foil. However, the exact value of C_{an} is not readily available for an oscillating plate. La Mantia and Dabnichki⁵⁵ numerically evaluated the added mass tensor for an oscillating NACA0012 foil, and the normal component of the added mass coefficient was estimated to be 0.795. Considering the analogy between the NACA0012 foil and the flat plate, we set $C_{an} = 0.795$ in the present estimation as well. Finally, the instantaneous added mass force in the global coordinate system can be calculated as

$$\begin{aligned} F_{ax} &= -F_{an} \sin(\theta), \\ F_{ay} &= F_{an} \cos(\theta). \end{aligned} \tag{17}$$

The thrust and lift coefficients due to the added mass ($C_{T,a}$ and $C_{L,a}$, respectively) can be computed according to Eqs. (3) and (4). To differentiate various force contributions, the total thrust and lift force

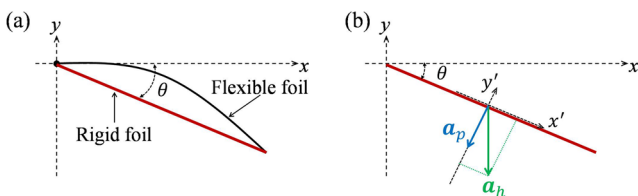


FIG. 19. Schematic views of the (a) simplified rigid foil and (b) the acceleration vectors.

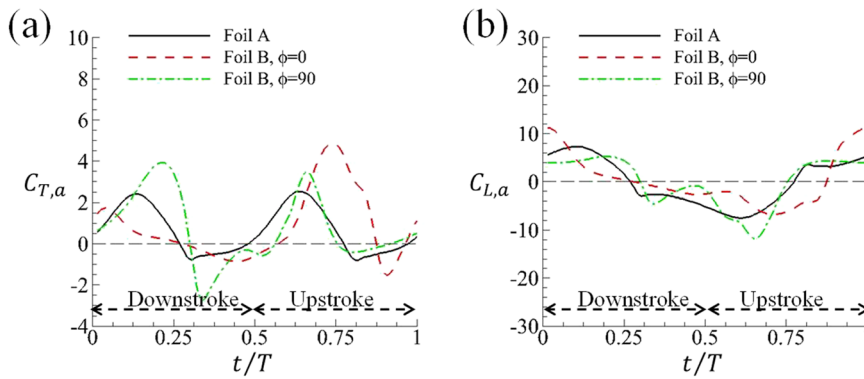


FIG. 20. Instantaneous (a) thrust and (b) lift forces due to added mass within one motion period at $\bar{K} = 1.42$ and $St_c = 0.5$. Foil A has constant stiffness, and foil B has time-varying stiffness.

coefficients are denoted hereafter as $C_{T,t}$ and $C_{L,t}$, respectively. The residual force coefficients are then defined as $C_{T,r} = C_{T,t} - C_{T,a}$ and $C_{L,r} = C_{L,t} - C_{L,a}$.

Figure 20(a) shows the time history of the thrust coefficient due to added mass. It is seen that the added mass force produces both thrust and drag for all three cases. By comparing Fig. 20(a) with Fig. 8(a), we find that the thrust coefficients of foil A and foil B at $\phi = 0^\circ$ due to added mass ($C_{T,a}$) follow similar variation patterns to the corresponding total thrust coefficients ($C_{T,t}$). Interestingly, foil B at $\phi = 90^\circ$ creates considerable thrust owing to added mass during the downstroke whereas little thrust is observed in Fig. 8(a),

indicating that significant drag force (negative $C_{T,r}$) is produced, which cancels the contribution of the added mass. Figure 20(b) illustrates the lift coefficients contributed by the added mass. It is observed that the variation patterns of $C_{L,a}$ are very different from those of the total lift coefficients ($C_{L,t}$). Specifically, the peaks created by foil B during the upstroke no longer exist.

Figure 21 summarizes the time-averaged coefficients of the total thrust force, the thrust force associated with added mass, and the residual thrust force (i.e., the different between these two) as functions of mean normalized bending stiffness. It is observed that for foil A [see Fig. 21(a)], the added mass contributes half of the total

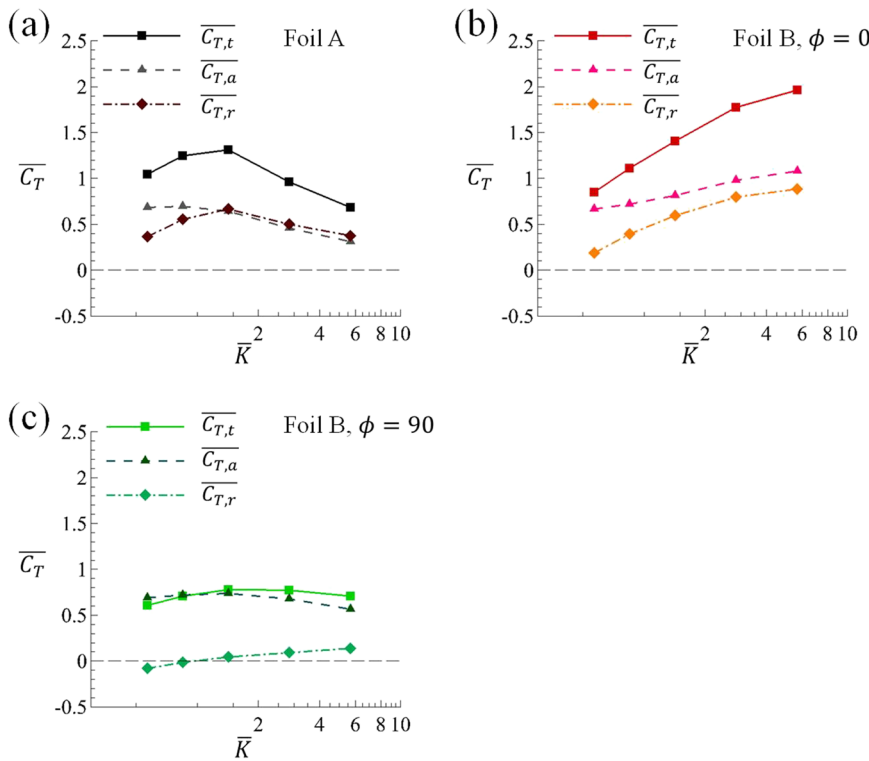


FIG. 21. Time-averaged coefficients of total thrust ($\overline{C_{T,t}}$), thrust due to added mass ($\overline{C_{T,a}}$) and the residual thrust ($\overline{C_{T,r}}$) at $St_c = 0.5$: (a) foil A, (b) foil B, $\phi = 0^\circ$, and (c) foil B, $\phi = 90^\circ$.

thrust force and the percentage increases even higher at smaller stiffness. For foil B at $\phi = 0^\circ$ [see Fig. 21(b)], the contribution from the added mass is more than 50% for all the flexibilities considered here. Different from the previous two cases, foil B at $\phi = 90^\circ$ [see Fig. 21(c)] generates thrust force almost solely using the added mass mechanism. In summary, for all three foils, the added mass contributes significantly (at least 50%) to the total thrust generation. The present findings agree with the study by Andro and Jacquin,⁵⁴ where a flapping NACA0012 foil at $Re = 1000$ was numerically investigated and three regimes were identified according to motion frequency. The first regime is a quasi-steady regime ($St_c < 0.1$), where the force is dominated by the leading edge vortices. The second regime is a transitional regime ($0.1 < St_c < 0.5$), where the force is mainly created by wake capture and a small portion of added mass contribution. The third one is an added mass regime ($St_c > 0.5$), where the acceleration force becomes the dominant factor. Considering the fact that the Strouhal number in the present study is $St_c = 0.5$, it is not a surprise that the added mass contributes more than half of the total thrust force.

V. CONCLUSIONS

In the present paper, the propulsion performance of a flexible heaving foil with time-varying stiffness was numerically investigated using a fully coupled fluid-structure interaction model. Compared with the foil with constant flexibility (foil A), the performance of the foil with time-varying stiffness (foil B) was significantly affected by the phase ϕ between the actuating motion and the time-changing flexibility. The best propulsion performance of foil B was achieved at $\phi = 0^\circ$, and the maximum time-averaged thrust coefficient was increased by $\sim 52\%$ compared with foil A. The highest propulsion efficiency accomplished by foil B was similar to that of foil A. The thrust enhancement may become more substantial when the scale of the wing is restricted.

Besides, the passive deformation of foil B was also considerably influenced by phase ϕ . The deformation of the foil was still at its first bending mode, but the patterns were no longer symmetrical. The non-symmetrical conformation further led to a deflected vortex-shedding pattern, which was believed to be the reason for the lift generation. In addition, foil B at $\phi = 0^\circ$ created larger relative deformation and higher pressure difference simultaneously during the upstroke, resulting in a surge of thrust force. However, the largest relative deformation and the highest pressure difference were accomplished during the downstroke and the upstroke, respectively, when ϕ is 90° , indicating that the exact deformation of the foil can significantly change the surrounding flow field and the flow dynamics, in return, will affect the force creation. This is reminiscent of a previous study²⁹ that the flapping wing flyers may adjust the kinematics and deformation instantaneously by sensing the pressure distribution to improve their performance. With a simplified model, it was found that the added mass of the foil contributed more than 50% of the total thrust force for both foil A and foil B. It is also realized that one of the limitations of the present study is that the heave amplitude and the frequency were fixed values. The effects of these variables on the dynamics of a foil with time-dependent flexibility and the optimization of the thrust and efficiency within a larger parameter matrix are subject to future research.

ACKNOWLEDGMENTS

Results were obtained using the ARCHIE-WeSt High Performance Computer (www.archie-west.ac.uk) based at the University of Strathclyde.

DATA AVAILABILITY

The data that support the findings of this study are available from the corresponding author upon reasonable request.

REFERENCES

- K. D. Jones and M. F. Platzer, "Design and development considerations for biologically inspired flapping-wing micro air vehicles," *Exp. Fluids* **46**(5), 799–810 (2009).
- W. Shyy, H. Aono, S. K. Chimakurthi, P. Trizila, C.-K. Kang, C. E. S. Cesnik, and H. Liu, "Recent progress in flapping wing aerodynamics and aeroelasticity," *Prog. Aerosp. Sci.* **46**(7), 284–327 (2010).
- I. Gursul, D. J. Cleaver, and Z. Wang, "Control of low Reynolds number flows by means of fluid-structure interactions," *Prog. Aerosp. Sci.* **64**, 17–55 (2014).
- M. S. Triantafyllou, A. H. Techet, and F. S. Hover, "Review of experimental work in biomimetic foils," *IEEE J. Oceanic Eng.* **29**(3), 585–594 (2004).
- M. F. Platzer, K. D. Jones, J. Young, and J. C. S. Lai, "Flapping wing aerodynamics: Progress and challenges," *AIAA J.* **46**(9), 2136–2149 (2008).
- I. H. Tuncer and M. F. Platzer, "Computational study of flapping airfoil aerodynamics," *J. Aircr.* **37**(3), 514–520 (2000).
- Q. Xiao and W. Liao, "Numerical investigation of angle of attack profile on propulsion performance of an oscillating foil," *Comput. Fluids* **39**(8), 1366–1380 (2010).
- J. H. J. Buchholz, A. J. Smits, J. H. J. Buchholz, and A. J. Smits, "On the evolution of the wake structure produced by a low-aspect-ratio pitching panel," *J. Fluid Mech.* **546**, 433–443 (2006).
- J. Han, Z. Yuan, and G. Chen, "Effects of kinematic parameters on three-dimensional flapping wing at low Reynolds number," *Phys. Fluids* **30**(8), 081901 (2018).
- P. Mancini, A. Medina, and A. R. Jones, "Experimental and analytical investigation into lift prediction on large trailing edge flaps," *Phys. Fluids* **31**(1), 013106 (2019).
- Y. Z. Lyu, H. J. Zhu, and M. Sun, "Aerodynamic forces and vortical structures of a flapping wing at very low Reynolds numbers," *Phys. Fluids* **31**(4), 041901 (2019).
- K. D. Jones, C. M. Dohring, and M. F. Platzer, "Experimental and computational investigation of the Knoller-Betz effect," *AIAA J.* **36**(7), 1240–1246 (1998).
- G. C. Lewin and H. Haj-Hariri, "Modelling thrust generation of a two-dimensional heaving airfoil in a viscous flow," *J. Fluid Mech.* **492**(492), 339–362 (2003).
- I. Gursul and D. Cleaver, "Plunging oscillations of airfoils and wings: Progress, opportunities, and challenges," *AIAA J.* **57**, 3648–3665 (2019).
- J. M. Anderson, K. Streitlien, D. S. Barrett, and M. S. Triantafyllou, "Oscillating foils of high propulsive efficiency," *J. Fluid Mech.* **360**, 41–72 (1998).
- J. Young and J. C. S. Lai, "Mechanisms influencing the efficiency of oscillating airfoil propulsion," *AIAA J.* **45**(7), 1695–1702 (2007).
- J. Young and J. C. S. Lai, "Oscillation frequency and amplitude effects on the wake of a plunging airfoil," *AIAA J.* **42**(10), 2042–2052 (2004).
- S. Heathcote, Z. Wang, and I. Gursul, "Effect of spanwise flexibility on flapping wing propulsion," *J. Fluids Struct.* **24**(2), 183–199 (2008).
- H. Dai, H. Luo, P. J. S. A. F. de Sousa, and J. F. Doyle, "Thrust performance of a flexible low-aspect-ratio pitching plate," *Phys. Fluids* **24**(10), 101903 (2012).
- F.-B. Tian, H. Luo, J. Song, and X.-Y. Lu, "Force production and asymmetric deformation of a flexible flapping wing in forward flight," *J. Fluids Struct.* **36**, 149–161 (2013).
- S. Heathcote and I. Gursul, "Flexible flapping airfoil propulsion at low Reynolds numbers," *AIAA J.* **45**(5), 1066–1079 (2007).

- ²²K. Shoele and Q. Zhu, "Performance of a wing with nonuniform flexibility in hovering flight," *Phys. Fluids* **25**(4), 041901 (2013).
- ²³A. K. Kancharala and M. K. Philen, "Optimal chordwise stiffness profiles of self-propelled flapping fins," *Bioinspiration Biomimetics* **11**(5), 056016 (2016).
- ²⁴S. Michelin and S. G. Llewellyn Smith, "Resonance and propulsion performance of a heaving flexible wing," *Phys. Fluids* **21**(7), 071902 (2009).
- ²⁵F. Paraz, L. Schouveiler, and C. Eloy, "Thrust generation by a heaving flexible foil: Resonance, nonlinearities, and optimality," *Phys. Fluids* **28**(1), 011903 (2016).
- ²⁶M. J. David, R. N. Govardhan, and J. H. Arakeri, "Thrust generation from pitching foils with flexible trailing edge flaps," *J. Fluid Mech.* **828**, 70–103 (2017).
- ²⁷C.-K. Kang, H. Aono, C. E. S. Cesnik, and W. Shyy, "Effects of flexibility on the aerodynamic performance of flapping wings," *J. Fluid Mech.* **689**, 32–74 (2011).
- ²⁸P. A. Dewey, B. M. Boschitsch, K. W. Moored, H. A. Stone, and A. J. Smits, "Scaling laws for the thrust production of flexible pitching panels," *J. Fluid Mech.* **732**, 29–46 (2013).
- ²⁹S. Ramananarivo, R. Godoy-Diana, and B. Thiria, "Rather than resonance, flapping wing flyers may play on aerodynamics to improve performance," *Proc. Natl. Acad. Sci. U. S. A.* **108**(15), 5964–5969 (2011).
- ³⁰S. Sunada, D. Song, X. Meng, H. Wang, L. Zeng, and K. Kawachi, "Optical measurement of the deformation, motion, and generated force of the wings of a Moth, *Mythimna Separata* (Walker)," *JSME Int. J., Ser. B* **45**(4), 836–842 (2002).
- ³¹J.-S. Chen, J.-Y. Chen, and Y.-F. Chou, "On the natural frequencies and mode shapes of dragonfly wings," *J. Sound Vib.* **313**, 643–654 (2008).
- ³²B. Yin and H. Luo, "Effect of wing inertia on hovering performance of flexible flapping wings," *Phys. Fluids* **22**(11), 111902 (2010).
- ³³Q. Zhu, "Numerical simulation of a flapping foil with chordwise or spanwise flexibility," *AIAA J.* **45**(10), 2448–2457 (2007).
- ³⁴M. Olivier and G. Dumas, "A parametric investigation of the propulsion of 2D chordwise-flexible flapping wings at low Reynolds number using numerical simulations," *J. Fluids Struct.* **63**, 210–237 (2016).
- ³⁵W. Shan, S. Diller, A. Tutcuoglu, and C. Majidi, "Rigidity-tuning conductive elastomer," *Smart Mater. Struct.* **24**(6), 065001 (2015).
- ³⁶C. Eloy, "Optimal strouhal number for swimming animals," *J. Fluids Struct.* **30**, 205–218 (2012).
- ³⁷B. E. Schubert and D. Floreano, "Variable stiffness material based on rigid low-melting-point-alloy microstructures embedded in soft poly(dimethylsiloxane) (PDMS)," *RSC Adv.* **3**(46), 24671–24679 (2013).
- ³⁸G. Shi, Q. Xiao, Q. Zhu, and W. Liao, "Fluid-structure interaction modeling on a 3D ray-strengthened caudal fin," *Bioinspiration Biomimetics* **14**, 036012 (2019).
- ³⁹W. Liao, J. Cai, and H. M. Tsai, "A multigrid overset grid flow solver with implicit hole cutting method," *Comput. Methods Appl. Mech. Eng.* **196**(9–12), 1701–1715 (2007).
- ⁴⁰A. Jameson, W. Schmidt, and E. Turkel, "Numerical solution of the Euler equations by finite volume methods using Runge Kutta time stepping schemes," in *AIAA 14th Fluid and Plasma Dynamics Conference*, 1981.
- ⁴¹A. Jameson, "Time dependent calculations using multigrid, with applications to unsteady flows past airfoils and wings," in *AIAA 10th Computational Fluid Dynamics Conference* (AIAA, 1991).
- ⁴²B. S. H. Connell and D. K. P. Yue, "Flapping dynamics of a flag in a uniform stream," *J. Fluid Mech.* **581**, 33–67 (2007).
- ⁴³C. Farhat and M. Lesoinne, "Two efficient staggered algorithms for the serial and parallel solution of three-dimensional nonlinear transient aeroelastic problems," *Comput. Methods Appl. Mech. Eng.* **182**(3–4), 499–515 (2000).
- ⁴⁴M. Sadeghi, F. Liu, K. L. Lai, and H. M. Tsai, "Application of three-dimensional interfaces for data transfer in aeroelastic computations," in *22nd Applied Aerodynamics Conference and Exhibit* (AIAA, 2004), pp. 1–30.
- ⁴⁵R. Mittal, H. Dong, M. Bozkurtas, G. Lauder, and P. Madden, "Locomotion with flexible propulsors: II. Computational modeling of pectoral fin swimming in sunfish," *Bioinspiration Biomimetics* **1**(4), S35 (2006).
- ⁴⁶G. Liu, Y. Ren, H. Dong, O. Akanyeti, J. C. Liao, and G. V. Lauder, "Computational analysis of vortex dynamics and performance enhancement due to body-fin and fin-fin interactions in fish-like locomotion," *J. Fluid Mech.* **829**, 65–88 (2017).
- ⁴⁷W. Liu, Q. Xiao, and F. Cheng, "A bio-inspired study on tidal energy extraction with flexible flapping wings," *Bioinspiration Biomimetics* **8**(3), 36011–36016 (2013).
- ⁴⁸W. Liu, Q. Xiao, and Q. Zhu, "Passive flexibility effect on oscillating foil energy harvester," *AIAA J.* **54**(4), 1172–1187 (2016).
- ⁴⁹R. G. Bottom II, I. Borazjani, E. L. Blevins, and G. V. Lauder, "Hydrodynamics of swimming in stingrays: Numerical simulations and the role of the leading-edge vortex," *J. Fluid Mech.* **788**, 407–443 (2016).
- ⁵⁰E. Konstantinidis, "Added mass of a circular cylinder oscillating in a free stream," *Proc. R. Soc. A* **469**, 20130135 (2013).
- ⁵¹J. Chen, W. O. Friesen, and T. Iwasaki, "Mechanisms underlying rhythmic locomotion: Body-fluid interaction in undulatory swimming," *J. Exp. Biol.* **214**, 561–574 (2011).
- ⁵²K. A. Harper, M. D. Berkemeier, and S. Grace, "Modeling the dynamics of spring-driven oscillating-foil propulsion," *IEEE J. Oceanic Eng.* **23**(3), 285–296 (1998).
- ⁵³S. P. Sane and M. H. Dickinson, "The control of flight force by a flapping wing: Lift and drag production," *J. Exp. Biol.* **204**, 2607–2626 (2001).
- ⁵⁴J.-Y. Andro and L. Jacquin, "Frequency effects on the aerodynamic mechanisms of a heaving airfoil in a forward flight configuration," *Aerosp. Sci. Technol.* **13**, 71–80 (2009).
- ⁵⁵M. La Mantia and P. Dabnichki, "Added mass effect on flapping foil," *Eng. Anal. Boundary Elem.* **36**, 579–590 (2012).